Solar Energy 208 (2020) 697–707

Contents lists available at ScienceDirect

Solar Energy

journal homepage: www.elsevier.com/locate/solener

Enhanced performance of planar perovskite solar cells using TiO_2/SnO_2 and TiO_2/WO_3 bilayer structures: Roles of the interfacial layers

Mozhgan Kazemzadeh Otoufi [a,b], Mehdi Ranjbar [a,*], Ahmad Kermanpur [c,*], Nima Taghavinia [d,e], Mehran Minbashi [f], Mozhdeh Forouzandeh [f], Firouzeh Ebadi [e]

[a] Department of Physics, Isfahan University of Technology, Isfahan 84156-83111, Iran
[b] Physics Group, Pardis College, Isfahan University of Technology, Isfahan 84156-83111, Iran
[c] Department of Materials Engineering, Isfahan University of Technology, Isfahan 84156-83111, Iran
[d] Department of Physics, Sharif University of Technology, Tehran 11155-9161, Iran
[e] Institute for Nanoscience and Nanotechnology, Sharif University of Technology, Tehran 14588-89694, Iran
[f] Department of Physics, Tarbiat Modares University, Tehran 14115-175, Iran

ARTICLE INFO

Keywords:
Perovskite solar cells
Electron transport bilayer
TiO_2
WO_3
SnO_2
Sputtering

ABSTRACT

In planar perovskite solar cells (PSCs), engineering the extraction and recombination of electron–hole pairs by modification of the electron transport layer (ETL)/perovskite interface is very vital for obtaining high performance. The main idea here is to improve properties of the TiO_2/perovskite interface by inserting an ultra-thin layer (UTL) of WO_3 or SnO_2 with the thickness of less than 10 nm by RF magnetron sputtering method. The structural and electrical characteristics of the samples were tested by XRD, AFM, FE-SEM, Mott-Schottky analysis, UV–Vis spectroscopy, J-V characterization and electrochemical impedance spectroscopy (EIS). It was found that the bilayer structured ETLs exhibit advantages of high electron extraction and low interfacial recombination together mainly based on a more effective energy level alignment. The best performance here belongs to the cell with TiO_2/SnO_2 bilayer by which an improved efficiency exceeding 12% was achieved for the planar PSCs. The role of SnO_2 and WO_3 UTLs was also modeled using SCAPS-1D software. This simulation supported the experimental results and was used to interpret the photovoltaic behaviors of the fabricated devices based on defect characteristics. The present work proposes a simple and promising method to make photovoltaic devices with desirable charge transport and recombination properties.

1. Introduction

Utilization of solar energy and its conversion into electricity, as the most convenient for use in modern life, is one of the major challenges of the twenty-first century. Demands for improving performance and cost-effectiveness of harnessing the solar energy has made it indispensable to get progress in photovoltaics. Perovskite solar cells (PSCs), composed of the organic-metal-halide materials, have shown enormous potential as cheaper alternatives to existing conventional solar cells. They have made impressive progress in maximum power conversion efficiencies (PCEs) from 3.8% to 25.2% in just one decade (NREL, 2019).

The electron transport layer (ETL) plays a significant role in achieving high efficiency in PSCs (Chen et al., 2018). The characteristics of the ETL, including its energy level alignment, trap states, charge mobility and morphology-dependent parameters, material and its related interface properties are very vital in PSCs performance (Yang et al., 2016b). Mesoporous ETLs (~150 nm) are normally used in the stable and highly efficient PSCs, but they offer a relatively complicated device fabrication and their large scale manufacturing by spin-coating is still challenging. Therefore, the planar device structure has attracted significant attention for its feasible and roll-to-roll manufacturing capability. However, the planar PSCs exhibit significantly lower PCE and higher hysteresis compared to the mesoporous-type PSCs, owing to defects in the ETL and direct contacts between the perovskite and FTO layers (Ding et al., 2018).

Many modifications have been applied on ETLs to improve the efficiency of planar PSCs such as doping, finding the best material, controlling physical properties, composition and interface engineering (El Haimeur et al., 2020; Mohammadian-Sarcheshmeh and Mazloum-Ardakani, 2018; Yang et al., 2016b). The interface engineering

* Corresponding authors.
E-mail addresses: ranjbar@iut.ac.ir (M. Ranjbar), ahmad_k@iut.ac.ir (A. Kermanpur).

https://doi.org/10.1016/j.solener.2020.08.035
Received 12 December 2019; Received in revised form 8 August 2020; Accepted 11 August 2020

includes adding the self-assembled monolayers (Yang et al., 2016b), ETL surface treatments (Ke et al., 2015; Li et al., 2015) and introducing the organic molecules (Yang et al., 2016a). Inserting a wide band gap metal oxide semiconductor (such as ZnO, SrO and MgO) ultra-thin layer (UTL) at ETL's interfaces has been also reported as a capable approach in improving electron extraction and suppressing charge recombination (Mohammadian-Sarcheshmeh and Mazloum-Ardakani, 2018; Yang et al., 2016b). There are examples of successfully building an effective band alignment (Kulkarni et al., 2016; Lu et al., 2017b; Xu et al., 2015), providing a base for better formation of the perovskite layer (Kogo et al., 2016), reducing the density of trap states (Lu et al., 2017b) and preventing the undesirable chemical interactions (Kulkarni et al., 2016) using this strategy.

The wide band gap semiconductors, SnO_2 and WO_3 can be good candidates to be used as UTLs for optimizing TiO_2-based planar PSCs. Compared to TiO_2, several advantages have been reported for SnO_2 such as faster electron extraction, better energy band alignment to perovskite and more efficient electron transfer ability as well as minimizing/eliminating degradation of PSCs (Christians et al., 2018). WO_3 is also a chemically stable semiconductor and compared to TiO_2, indicates higher electron mobility (10–20 $cm^2 \cdot V^{-1} \cdot s^{-1}$), better transparency and a faster kinetic process of charge transfer at its interface with perovskite layer (Wang et al., 2015).

Accordingly, the main idea of this paper is to develop TiO_2/SnO_2 and TiO_2/WO_3 bilayers as ETLs by the precise, reproducible and industry compatible method of RF-sputtering and investigate how combining the merits of these oxide films affect the photovoltaic performance of TiO_2-based planar PSCs. This study can be of benefit for both efficiency improvement and further realization of the electron transport mechanism in planar PSCs. To further confirm the photovoltaic behaviors, the J-V results were compared using both spin-coated (SC) and RF-sputtered (RF) TiO_2 compact layers (CLs). Furthermore, the UTLs were examined with different thicknesses of 4 and 10 nm. A simulation work was also performed on the most efficient cells to obtain a deeper insight to device electrical properties. Finally, it was found that with these interfacial bilayers, photovoltaic characteristics and cell performance were improved noticeably.

2. Materials and experimental procedures

2.1. Cell preperation

2.1.1. Preparation of glass substrates

F:SnO_2 (FTO) substrates (Solaronix TCO22-15) were chemically etched with zinc powder and 2 M HCl solution and then cleaned through washing the substrates in several stages of sonication in soap solution, 0.2 M HCl solution in ethanol, acetone, ethanol and isopropanol for 10 min respectively and then dried in an oven of 120 ℃ for 30 min. All substrates were further cleaned by heating at 500 ℃ for 30 min.

2.1.2. Deposition of TiO_2, SnO_2 and WO_3 layers

RF TiO_2 CLs were deposited using Ti target (99.5%, 2 in. in diameter, 5 mm thick) (Loterios, Italy). Deposition by RF-sputtering method was conducted after 10 min pre-sputtering in a DST3-T magnetron sputtering instrument (Nano-Structured Coatings Co.). The atmosphere in the chamber was made of Ar as inert gas and a partial pressure of O_2 as reactive gas where their flows were set by MFC at 4 and 2 sccm, respectively. The total working pressure was 1.05×10^{-2} Torr in the sputtering chamber. The sputtering power was 100 W, the substrate temperature was 200 °C and the distance between substrate and target was 7 cm.

In case of depositing SnO_2 layers, the parameters of RF-sputtering deposition method were same as TiO_2 CLs except for applying a ceramic target of SnO_2 (99.99%, 2 in. in diameter, 3 mm thick, Sindlhauser Materials GmbH, Germany).

WO_3 layers were also deposited by RF-sputtering method similarly with these differences that a W target (99.95%, 2 in. in diameter, 0.5 mm thick, Plansee, Germany) was used, the Ar and O_2 flows were equally kept 4 sccm during deposition and the total pressure in the chamber became 1.18×10^{-2} Torr in this case.

In this work, TiO_2-CL, TiO_2-CL/SnO_2-UTL and TiO_2-CL/WO_3-UTL were the different studied ETL architectures (Fig. 1(a)). After depositing each of the oxide layers, a 30 min heating process at 500 °C was conducted. There are reports introducing 500 °C as the optimum temperature for annealing the ETLs of SnO_2 (Qiu et al., 2018), TiO_2 (Huang et al., 2017; Lu et al., 2017a) and WO_3 (Eze et al., 2017). As another effective factor, controlling the layers thicknesses play an important role in device performance (Mohammadian-Sarcheshmeh and Mazloum-Ardakani, 2018). We tried to obtain 50 nm TiO_2 CLs, since it has been found as an optimized size for this electron transport compact layer according to literature (Noh et al., 2018; Xu et al., 2015). In bilayer cases, the best performances have been achieved with UTLs of >10 nm thick (Xu et al., 2015; Yang et al., 2016b). Therefore, the interfacial effects of 4 and 10 nm UTLs were investigated here. The thickness was controlled by adjusting time with keeping all other sputtering parameters fixed during a layer deposition process. Using cross-sectional FE-SEM images of several samples, the deposition rate was measured to be ~3 Å/s, 1 Å/s and 0.13 Å/s for SnO_2, WO_3 and TiO_2, respectively. The deposition rates were confirmed by cross sectional FE-SEM images (Fig. S1) and found to be independent of substrate.

2.1.3. Preparation of TiO2 by spin coating (SC)

SC TiO_2 CLs were prepared by spin-coating method (2000 rpm) on the pre-treated FTO substrates with 30 s deposition time. In this deposition stage, a 0.15 M Titanium *iso*-propoxide (TTIP-Merck 97%) solution in anhydrous ethanol was normally used. Then a heating process at 500 °C for 30 min was carried out to prepare a severely attached TiO_2 CL on the FTO surfaces.

2.1.4. Cs/MA/FA perovskite precursor solution and film deposition

The perovskite layer with $Cs_{0.05}(MA_{0.17}FA_{0.83})_{0.95}Pb(I_{0.83}Br_{0.17})_3$ formula was deposited on the ETLs via one step deposition method. The precursor solution was prepared by adding FAI ($CH(NH_2)_2I$) (1 mmol) (Dyesol 98%), PbI_2 (1.5 mmol) (TCI 99.99%), MABr (CH_3NH_3Br) (1 mmol) (Dyesol 98%), and $PbBr_2$ (1.5 mmol) (IRASOL 99.99%) to N–N-dimethylformamide (DMF-Merck 99.5%) and dimethyl sulfoxide, (DMSO-Merck 99.9%) mixed anhydrous solvent (DMF:DMSO, 4:1 vol ratio). Then 50 μl of CsI solution containing CsI (1.5 mmol) (Sigma-Aldrich 99.999%) in DMSO (1 ml) was dissolved in 950 μl of aforementioned solution. This triple cation perovskite solution was then spin-coated on FTO/ETL substrates at 1000 rpm/10 s and 6000 rpm/30 s. In the last 15 s, 200 μl anti-solvent Ethyl acetate solution was poured slowly and layers were then quickly heated at 100 °C for 50 min.

2.1.5. Deposition of hole transport layer and top electrode

The Spiro-OMeTAD hole transport layer (HTL) was over-deposited by a 5000 rpm/30 s spin-coating process. The precursor solution was prepared by adding 72.3 mg of Spiro-OMeTAD (99.0%) in 1 ml of chlorobenzene (Merck 99%), 17.5 μl of a 520 mg mL^{-1} solution of lithium bis(trifluoromethylsulfonyl)imide (Li-TFSI) (Sigma-Aldrich 99.5%) in acetonitrile and 28.8 μl of 4-*tert*-butylpyridine (TBP,Sigma-Aldrich 96%). Finally, 80 nm Au metallic contact was deposited in a high vacuum chamber using a DTT thermal evaporation instrument (Nano-Structured Coatings Co.).

2.2. Characterizations

The X-ray diffraction patterns were measured using an ASENWARE AW-DX300 equipment with Cu K_α ($\lambda = 1.542$ Å) radiation. Scanning electron microscopy (SEM) images were observed applying a TESCAN–Mira3 fieldemission scanning electron microscope (FE-SEM). UV − vis absorption spectroscopy was performed using a Perkin Elmer

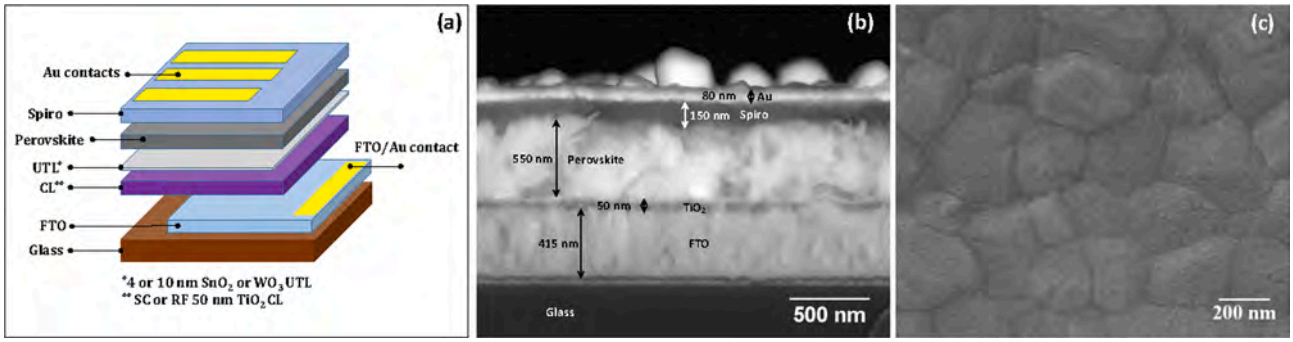

Fig. 1. (a) Schematic diagram of the device structure, (b) FE-SEM image of the cross section of SC TiO_2 based cell; (c) top view FE-SEM image of the perovskite layer.

Lambda 25 spectrophotometer. Atomic force microscope (AFM) measurements were obtained with ENTEGRA AFMNT – MDT and analyzed by Nova 1.0.26.1441 Pro. The Mott-Schottky analysis was taken in a quartz cell filled with 0.5 M Na_2SO_4 solution (pH 6.0) applying a Metrohm-Autolab potentiostat system with three-electrode configuration. The working, counter and reference electrodes were the fabricated metal oxide/FTO, Pt and Ag/AgCl (3 mol/kg KCl), respectively. The deposited metal oxide electrode included SnO_2, WO_3, RF TiO_2, or SC TiO_2 films with 50 nm thickness coated on FTO substrates for which the exposed areas where 0.65, 0.56, 0.78 and 0.75 cm^2, respectively. The frequency of the signal was 1000 Hz and scanning was done at dark with speed of 50 mV/s. All the above mentioned characterizations were performed on the layers after a 500 °C/30 min annealing process.

Measurements of incident photon-to-current conversion efficiency (IPCE) were performed utilizing a Sharif Solar IPCE-015 equipment. The photocurrent-voltage analyses were carried out by a Sharif Solar SIM-1000 system under AM 1.5 (100 mW/cm^2) (1 sun) simulated light radiation (calibrated by a Thorlabs photodiode). The J–V curves were recorded with the scan rate of 5 mV s^{-1} by a Keithley 2400 source meter. A mask with an open area of 0.09 cm^2 was used for masking the active area of the cells in these measurements. Electrochemical impedance spectroscopy (EIS) spectra were recorded using an Ivium, Compactstat potentiostat/galvanostat equipment.

3. Results

3.1. Structural, optical and electrical properties of ETLs

The surface morphology of TiO_2 CL/SnO_2 (4 nm) and TiO_2 CL/WO_3 (10 nm) bilayers on FTO by FE-SEM and AFM before and after modification by UTLs are shown in Fig. 2(a–d). Both the UTLs and TiO_2 CLs in the bilayer structures were deposited by RF-sputtering. A comparison of Fig. 2(a) with (b,c) reveals that the modified surfaces seem to have more uniform and sticking grains. Therefore, reduced grain boundaries and improved crystallinity, hence better conductivity (please refer to R_S values measured by EIS analysis), are expected for the modified CLs, facilitating the charge transport (Bu et al., 2017; Wang et al., 2017; Xu et al., 2015). The RMS surface roughness was measured to be 13.2 nm before modification, which reduced to about 10.5 nm after modification by both kinds of UTLs. The surface uniformity also improves the perovskite to ETL adhesion, and as a result, provides a better charge extraction and transport (Choi et al., 2016; Huang et al., 2017). From Fig. 2(a) and (d), clearer hence better crystallinity of the surface grains is observed for the RF TiO_2 CL compared to the SC layer. However, the spin coated TiO_2 CL Fig. 2(d) exhibits more uniform cloudy coverage with less RMS roughness of 12.0 nm. The smaller RMS roughness can be due to rotating of substrate during spin-coating, while this option was not available in the sputtering method.

The presence of the different UTLs was more investigated by energy dispersive X-ray spectroscopy (EDX) (Figs. S2(a-d)). From the figure and the inset tables, the addition of WO_3 or SnO_2 has led to the appearance of W peaks or the Sn atomic ratio enhancement, respectively. The elemental proportion of O has been increased as well. The chemical composition of these layers could not be determined by EDX analysis as the beneath layers contributes to the signals.

The XRD characterization results of the fabricated layers are given in Fig. S3 and Table S1. Fig. S3(a) shows diffraction patterns of 50 nm SnO_2, WO_3 and TiO_2 films without sign of other oxide impurities. Fig. S3 (b) shows the XRD pattern of the fabricated perovskite layer for which the $Cs_{0.05}(MA_{0.17}FA_{0.83})_{0.95}Pb(I_{0.83}Br_{0.17})_3$ formula with perovskite structure is proved comparing with other reports (Saliba et al., 2016). This characterization along with the cross sectional FE-SEM image of the fabricated PSC (Fig. 1(b)) and the top view image of the coarse grained perovskite layer (Fig. 1(c)), demonstrates the formation of high quality perovskite layer (Gedamu et al., 2018).

Fig. 3(a) shows the UV–Vis transmittance spectra of the different deposited TiO_2 based ETLs on FTO. From the spectra, the transmittances of the discussed ETLs all exceed 80% in the whole visible region, which favors the sufficient absorption of light by the perovskite (Wang et al., 2015). Therefore, the treatment of the TiO_2 layer does not affect the transmittance due to the very small thickness of WO_3 or SnO_2. Moreover, the peak and valley in the spectra reveals a good layer smoothness and uniformity (Swanepoel, 1984). It is known that the ETL band gap is an important factor seriously influences the cell performance. Therefore, using the UV–Vis data, the band gap of the fabricated 50 nm CLs was calculated based on the Tauc equation (Fig. 3(b)):

$$\alpha h\nu = B\left(h\nu - E_g\right)^m \tag{1}$$

In Eq. (1), m = 2 for allowed indirect and m = 1/2 for allowed direct transitions. For WO_3 and TiO_2, the best linear fitting was achieved taking m = 2, which is in agreement with other reports for 500 °C annealed WO_3 (Ganbavle et al., 2014) and TiO_2 (Lim et al., 2014; Reyes-Coronado et al., 2008). The calculated band gaps of the layers are presented in Table 1. The band gap of SnO_2 could not be calculated as it shows no absorption shoulder.

Fig. 4 shows the Mott-Schottky plots of the 50 nm TiO_2, SnO_2 and WO_3 thin films on FTO. The positive slope of the curves indicates that they are n-type semiconductors. The N_D and V_{fb} is calculated using the Mott-Schottky equation:

$$\frac{1}{C^2} = \frac{2}{\varepsilon_0 \varepsilon_r e N_D}\left(V - V_{fb} - \frac{kT}{e}\right) \tag{2}$$

in which e, ε_r, ε_0, V_{fb}, V and N_D are electron charge, dielectric constant of semiconductor, vacuum permittivity, flat band potential, applied potential and carrier concentration, respectively (Li and Wu, 2015). It is also possible to specify the position of the conduction band minimum based on the Eq. (3), using the N_D and the flat band values:

$$E_C = V_{fb} + kT\ln\left(\frac{N_D}{N_C}\right) \tag{3}$$

where N_C is the effective density of states in conduction band. Then the

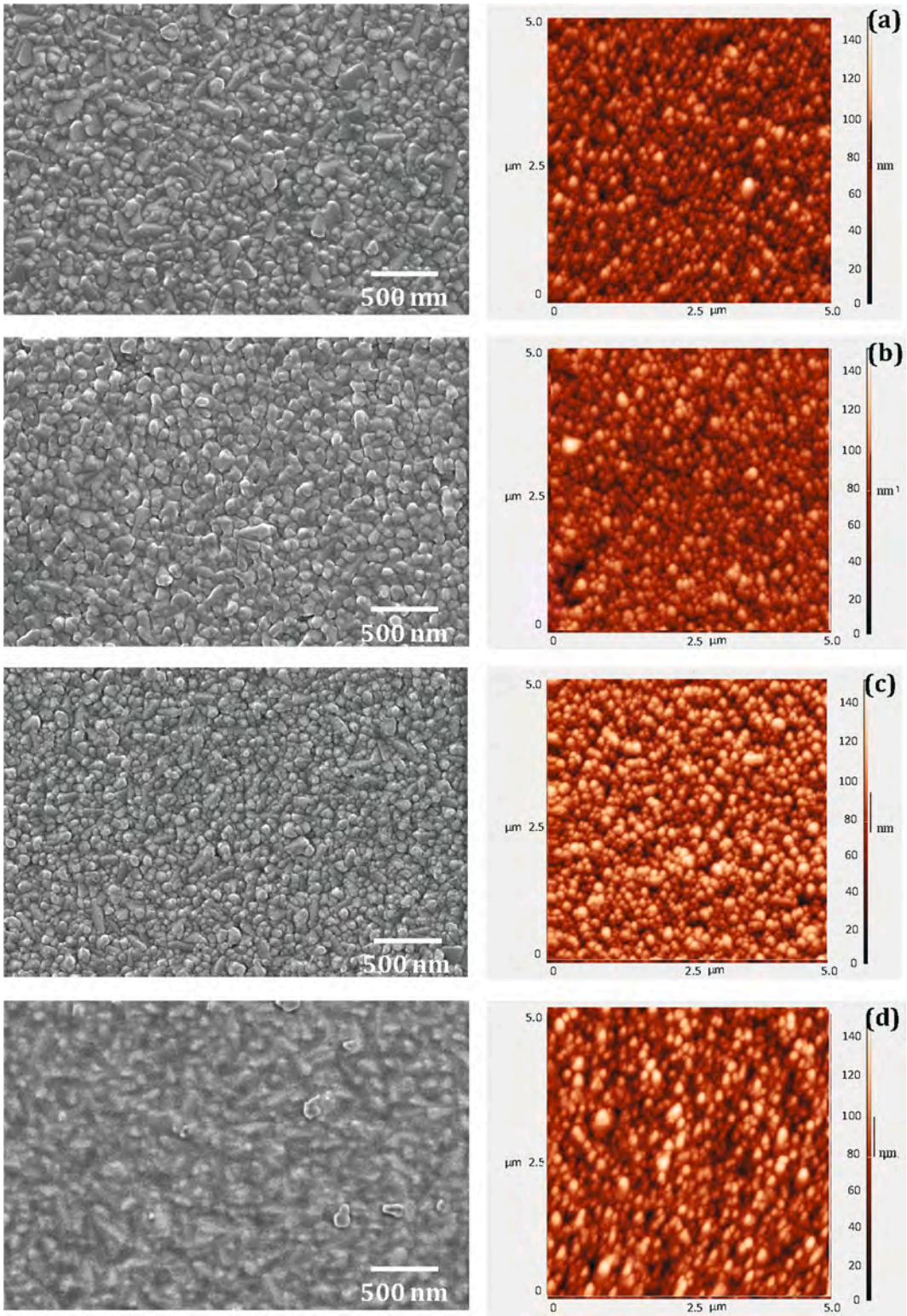

Fig. 2. Top view FE-SEM and AFM (5 µm_5 µm) images of (a) the bare RF TiO_2 CL film, (b) TiO_2 CL/SnO_2 UTL and (c) TiO_2 CL/WO_3 UTL bilayers as well as (d) the bare SC TiO_2 film.

valance band maximum is then achieved by inserting the calculated E_C and band gap into $E_V = E_C - E_g$ equation (Haghighi et al., 2018). The energy band edges calculated based on the Mott-Schottky and UV–Vis results are presented in Table 1, which is used to sketch the band alignments. In addition, the measured N_Ds and V_{fb}s as well as the input values of ε_r and Nc for Mott-Schottky calculations (Eqs. (2), (3)) can be found in Table S2.

The electron transport ability of the modified and unmodified TiO_2 CL was also comparatively evaluated by the photoluminescence (PL) measurements (Fig. S4). It was found that the bilayer structured ETLs exhibit an obvious PL quenching, suggesting higher electron extraction ability, due to the conduction band edge upshift and also enhanced

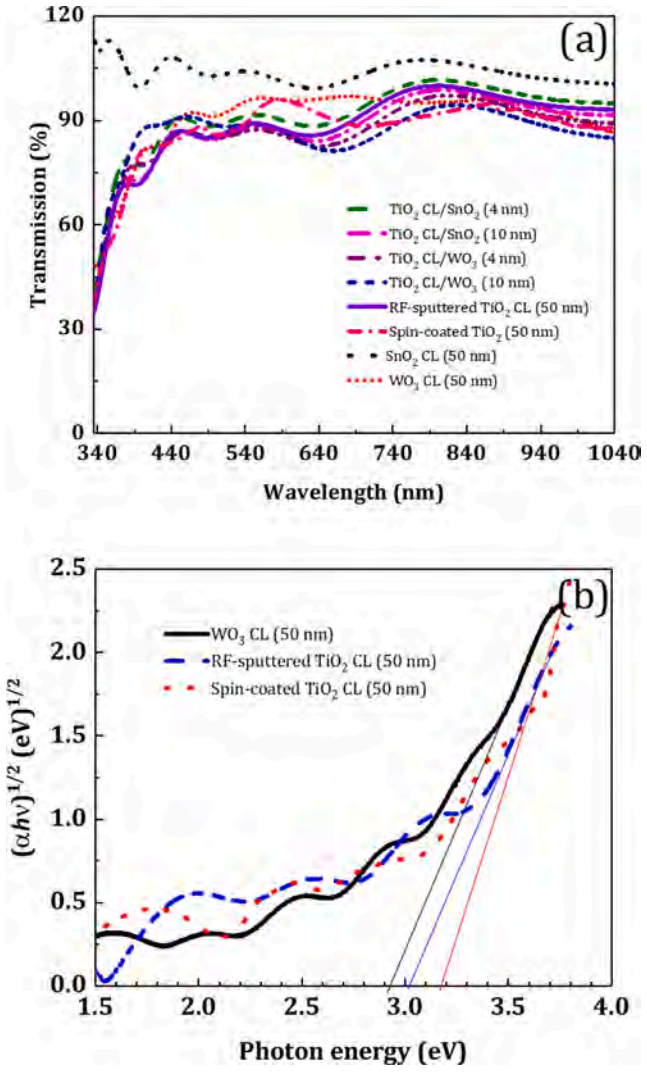

Fig. 3. (a) UV–Vis spectra of the single layers and RF TiO_2 based bilayers, (b) Tauc plots of the fabricated metal oxide semiconductors.

Table 1
The measured energy band edges of the fabricated metal oxide semiconductors.

E_V (eV)	E_g (eV)	E_C (eV)	Layer
−8.09	3.20	−4.89	SC TiO_2
−7.95	3.01	−4.94	RF TiO_2
−8.19	3.50*	−4.69	SnO_2
−7.51	2.92	−4.59	WO_3

* Based on Ref. (Qiu et al., 2018).

interface area between perovskite and ETL. Interestingly, a further degree of PL quenching has been achieved with SnO_2 UTL, indicating the most impactful electron picking up as a result of the more efficient energy band alignment.

3.2. Photovoltaic properties of the devices

Fig. 5(a,b) show J-V curves for the champion cells with RF SnO_2 and WO_3 UTLs (4 and 10 nm) on 50 nm SC or RF TiO_2 CLs, respectively. Table 2 depicts the corresponding calculated device parameters. The statistics of the measured devices is also revealed in Fig. S5. Since the backward (BW) scans provide efficiencies higher than the forward (FW) scans, the following focuses mainly on the reverse scan parameters. From the figure and table, embedding of the UTLs affects the J-V characteristics of the cell in a same manner for both SC and RF TiO_2 CLs. One point is that PCE increases by this modification and the thinner UTLs of 4 nm have greater effect on the efficiency compared to 10 nm UTLs. In addition, the SnO_2 UTLs improve the PCE further than the WO_3 UTLs, enhance the J_{SC} while keep the V_{OC} almost unaffected. Besides, one can see that although the WO_3 UTLs reduce the V_{OC}, they significantly enhance the J_{SC} so that the efficiency overall feature improves. As these findings could be observed for each TiO_2 deposition techniques, the effective role of our UTLs on J-V parameters is better confirmed.

Form Table 2 it can be observed that SC TiO_2 layers exhibit better PCE values. However, independent of the deposition method, the relatively low PCE in bare TiO_2 cells is mainly due to the lower J_{SC} values, regarding that V_{OC}s of the UTL containing cells are not greater. Moreover, a serious hysteresis accompanied by a strange bending is also observed in J-V curve of the bare SC TiO_2 cell in the 0–600 mV range. This kind of bending/hysteresis has been also reported elsewhere for the PSCs made by bare SC TiO_2 CLs, attributed to the slow extractions of charges and their accumulation at the interfaces (Lu et al., 2017b; Xu et al., 2015). Accordingly, our data with the existing reports suggest it is likely that the unmodified bare TiO_2 CL is not suitable for planar PSCs.

Our J-V results also represent the impact of the deposition layer method and UTL modification material on the hysteresis behavior. Table S3 depicts the calculated hysteresis index of the cells corresponding to Fig. 5. It can be seen that the RF TiO_2 based cells show a significantly lower hysteresis, which could be due to the better crystallinity of the CLs deposited by the sputtering technique (see Fig. 2) (Chen et al., 2016). Furthermore, the WO_3-UTL cells show an overall less hysteresis effect, especially for 10 nm thickness, compared to the SnO_2-UTL cells, which can be attributed to the better quality of the perovskite absorber layer according to literature (Gheno et al., 2017).

The J-V results reveal special photovoltaic behaviors for WO_3 PSCs. It can be seen that although WO_3 UTLs reduce the V_{OC}, it considerably increases the J_{SC}, which eventually leads to cell's efficiency enhancement. This effective role of WO_3 UTL on the efficiency and J_{SC} improvement was tested and confirmed again by comparison of IPCE measurement for the two cells with and without WO_3 UTL (Fig. S6). By integration over the whole spectra in this figure, we calculated J_{SC} to be 19.61 and 8.73 mA/cm^2, which confirms almost the data reported in Table 2. These distinctive J-V characteristics are similarly observed for the planar PSCs containing the bare WO_3 CL compared to those including TiO_2 or SnO_2 CL (Fig. S7). The WO_3 PSCs also remarkably reveal a further degree of degradation (Fig. S8(a,b)). From the figure, the WO_3-UTL cell shows 34% efficiency decay after two weeks, while it is 21% and 10% for the SnO_2-UTL and bare TiO_2-CL cells, respectively. The dark J-V curves of the RF TiO_2 based PSCs has been also shown in Fig. S9(a). It can be seen that a kind of step is observed in the dark J-V curves of the cells with a WO_3 UTL. For more investigation, the dark J-V curves of some other comparative cells fabricated and studied in our research has been also indicated in Fig. S9(b). This step is also observed in other dark J-V curves of the cells containing a WO_3 thin or ultra-thin layer while the dark J-V curves of those with SnO_2 or/and TiO_2 layer do not show such a behavior.

To further study the role of the inserted UTLs in the performance of planar PSCs, electrochemical impedance spectroscopy (EIS) curves were recorded for the most efficient cells (the SC TiO_2 based champion cells), at V_{OC} under 1 sun illumination (Guerrero et al., 2016). This result is useful for tracking the transport and recombination dynamics of internal carriers and for quantifying the parameters of charge transport, such as chemical capacitance, recombination resistance, and charge conductivity in planar PSCs (Chandiran et al., 2014). Fig. 6 indicates the Nyquist diagrams of the PSCs with the studied ETL types based on TiO_2 CL. It can be seen that all the diagrams consist of one pronounced arc in low frequency region in addition to a small arc at high frequencies. A simulated circuit model, obtained by the Zview software, fits the Nyquist plots (inside Fig. 6). The high-frequency small arc (left side) radius is directly proportional to the charge transport resistance (R_{CT}) at the

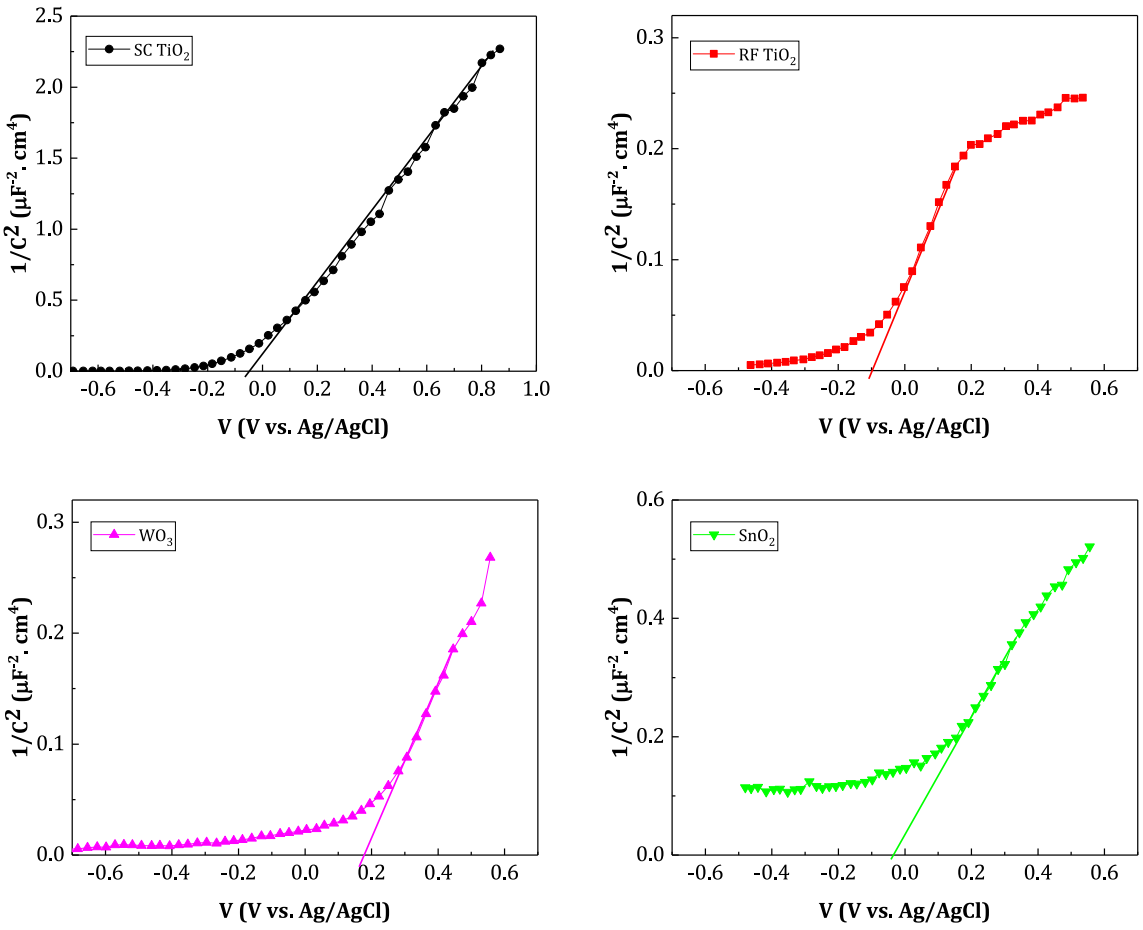

Fig. 4. Mott-Schottky analysis of the fabricated metal oxide semiconductors with 50 nm thickness coated on FTO substrates.

perovskite/ETL interface (Huang et al., 2017). While the low frequency arc (right side) is a transmission line with radius proportional to recombination resistance, R_{rec}, (inversely proportional to the recombination rate) at the perovskite/ETL interface (Huang et al., 2017). Table 3 depicts the calculated fitted values. From the inset circuits, a CPE (constant phase element) is used instead of C (capacitor) to model the depressed recombination semi-circles for the modified cells. This is attributed to the bilayer structures causing a double-layer capacitance, which appears as a CPE (Barsoukov and Macdonald, 2005). Since the cells differ only in the UTLs, any change in the EIS parameters, specially R_{CT} and R_{rec}, can be related to the difference in the ETL/perovskite interface. This is more distinctively observed in the corresponding capacitance-frequency diagram (Fig. S10) in which the plots overlap in high frequency range and separate in low frequency range (Guerrero et al., 2016).

From the inset of Fig. 6 and Table 3, it can be claimed that PSCs containing TiO_2/SnO_2 bilayers have lower charge transfer resistance, R_{CT}, compared to UTL free bare TiO_2 cell which could be partially due to an increased adhesion between the perovskite and composite layers (see the AFM images). This allows for more efficient extraction of the photogenerated electrons (Lu et al., 2017b). On the other hand, a larger energy gap between TiO_2 and the perovskite absorber in the bare TiO_2-based creates a larger energy barrier (Fig. 7) for electron transfer hence a larger R_{CT} (Huang et al., 2017). Inserting a the UTLs upshift the band edge and reduce the R_{CT} (Huang et al., 2017). It can be also noted that increasing the thickness of UTLs from 4 to 10 nm leads to larger R_{CT}s as it prolongs the perovskite to TiO_2 layer charge diffusion length, declines the carrier transfer and increases the interface charge accumulation (Lu et al., 2017b).

Based on the right semicircles, the effect of the UTLs on the recombination resistance of the cells is determined. Comparison of the EIS curves shows that bare TiO_2 cell has a strong charge recombination, due to smaller radius hence lower R_{rec} (Table 3). It can be clearly seen that R_{rec} increases in the presence of UTLs, meaning that the recombination rate has been reduced. It is likely that in the absence of UTLs, randomly diffused carriers gather and recombine at the ETL/perovskite interface and, as a result, R_{rec} decreases (Huang et al., 2017). When a UTL is introduced between perovskite and ETL, the photogernated charges transfer more effectively and then the recombination is sharply suppressed. As a result, in case of TiO_2/SnO_2 ETLs, the reduced R_{CT} and increased R_{rec} imply more efficient extraction/transport of the electrons leading to increased J_{SC} and PCE for these bilayer structured planar PSCs.

Another interesting point is that value of the starting point at the real part of the Nyquist plot corresponds to the series resistance R_S (Guerrero et al., 2016). The value of R_S is determined by the resistance of the FTO substrate, external wires, and other additional contributions. Other reports demonstrate that the ETL also have an effect on R_S (Gonzalez-Pedro et al., 2014). From Fig. 6, it is observed that the RS of all TiO_2 based devices are approximately the same as well as expected since the presence of a UTL with a low thickness introduces a negligible resistance. The little reduction in R_S values (Table 3) can be attributed to the improved adhesion between perovskite and the bilayers.

3.3. *Efficiency enhancement mechanism*

The efficiency enhancement achieved by inserting the UTLs of SnO_2 or WO_3 can be interpreted by two different strategies. One reason for the improvement of J_{SC} and subsequently PCE as well as electron extraction is considered owing to the improved adhesion between perovskite layer

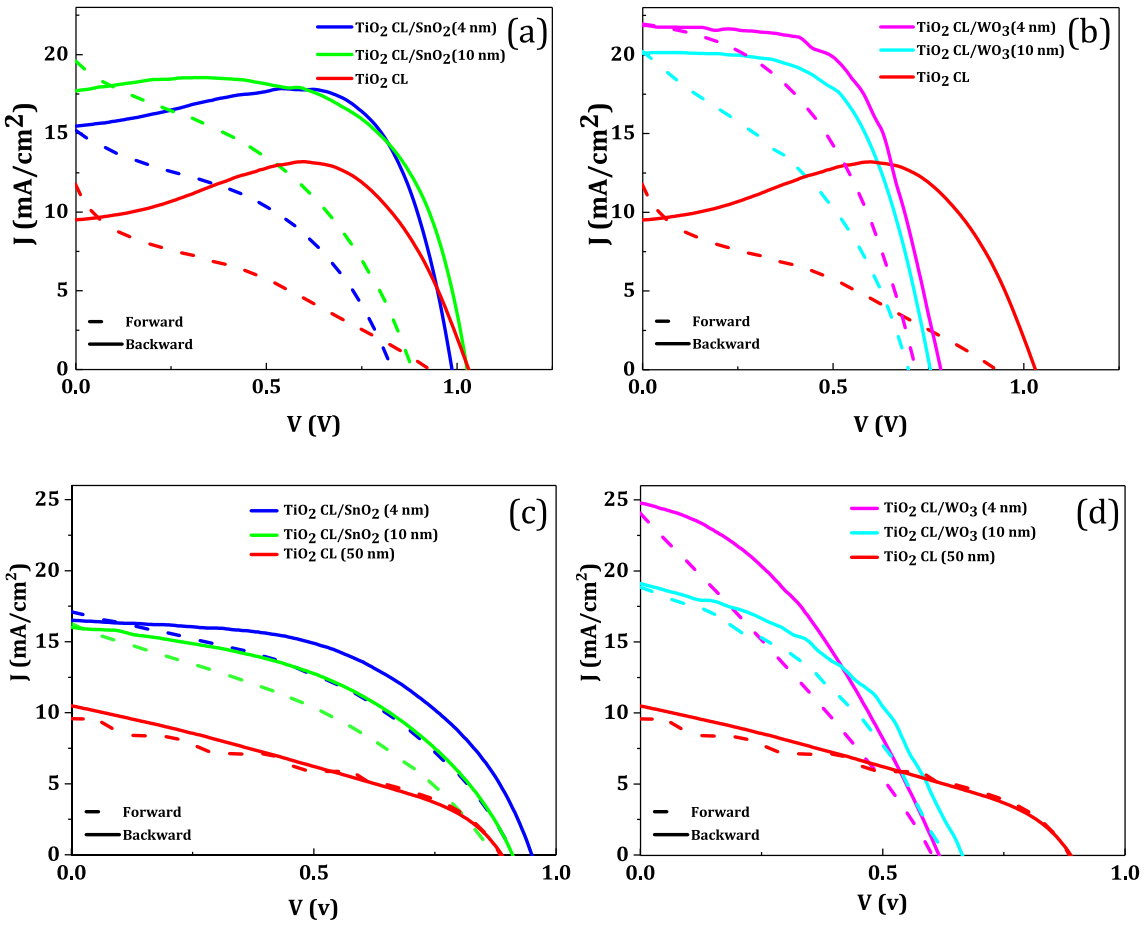

Fig. 5. J–V characteristics of the champion devices based on (a,b) SC TiO_2 and (c,d) RF TiO_2 with (a,c) SnO_2 UTL and (b,d) WO_3 UTL, under 1 sun illumination.

Table 2
Photovoltaic parameters of the TiO_2 based champion PSCs.

UTL	TiO_2 CL	Scan direction	J_{sc} (mA/cm^2)	V_{OC} (V)	FF	PCE (%)
SnO_2 (4 nm)	SC	BW	15.45	0.99	0.80	12.30
		FW	21.03	0.83	0.30	5.25
	RF	BW	16.74	0.95	0.52	8.23
		FW	17.11	1.00	0.39	6.65
SnO_2 (10 nm)	SC	BW	17.68	1.03	0.66	11.96
		FW	19.61	1.10	0.32	6.97
	RF	BW	16.42	0.91	0.45	6.71
		FW	16.30	1.00	0.32	5.23
WO_3 (4 nm)	SC	BW	21.88	0.78	0.60	10.24
		FW	22.16	0.71	0.46	7.26
	RF	BW	25.21	0.62	0.38	5.82
		FW	24.08	1.00	0.17	4.01
WO_3 (10 nm)	SC	BW	20.10	0.75	0.60	9.10
		FW	21.96	1.10	0.30	5.30
	RF	BW	19.98	0.66	0.41	5.50
		FW	18.87	0.62	0.39	4.64
no UTL	SC	BW	10.45	1.03	0.75	8.18
		FW	11.55	0.88	0.33	3.42
	RF	BW	10.48	0.89	0.34	3.16
		FW	9.58	0.89	0.37	3.12

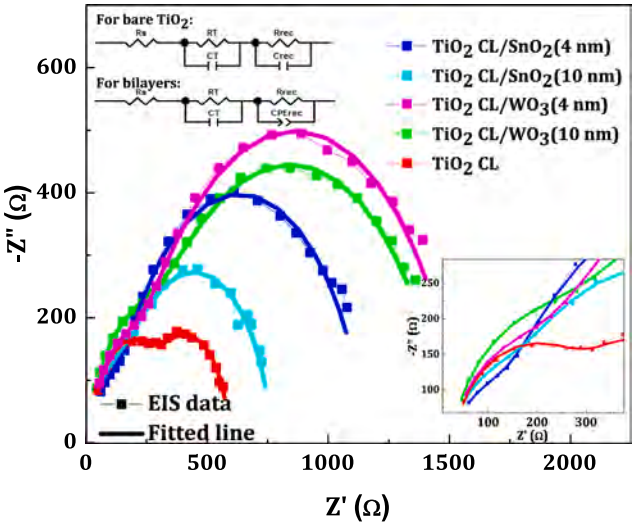

Fig. 6. Nyquist plot of the PSCs using different TiO_2 based ETLs. The equivalent circuits of this study as well as the zoomed feature of the high frequency semicircles are shown in the inset. CPE denotes constant phase element, and C denotes capacity.

and the bilayer with less interfacial trap states, facilitating charge extraction and reducing carrier recombination (Huang et al., 2017). The significant differences in film morphology as discussed in Fig. 2 (AFM and SEM) can be one of the origins. On the other hand, more effective band alignment of cells with UTLs of SnO_2 or WO_3 is likely the main root of the improved electron transport.

Scheme 1(a,b) shows the schematics of energy band alignment in the TiO_2-based bilayer structured PSCs based on the UV–Vis and Mott-Schottky results (Table 1). It reveals that both the VBM (valence band maximum) and CBM (conduction band minimum) of WO_3 (Scheme 1(a))

Table 3
Fitted resistance values calculated based on EIS measurements.

Resistance	SnO_2 (4 nm)	SnO_2 (10 nm)	WO_3 (4 nm)	WO_3 (10 nm)	no UTL
$R_{CT}(\Omega)$	98	134	166	207	270
$R_{rec}(\Omega)$	1043	614	1373	1274	290
R_S	19	19	18	16	28

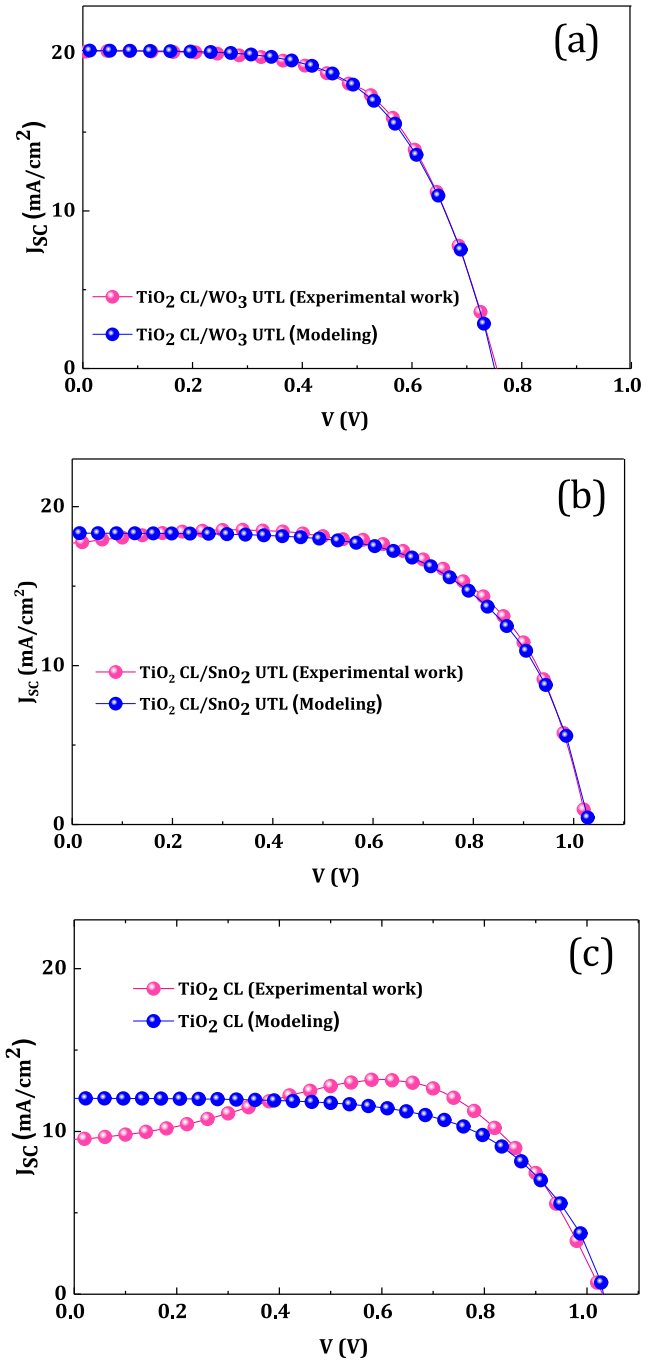

Fig. 7. The experimental and simulated diagrams of the TiO_2 based cells with (a) WO_3 UTL, (b) SnO_2 UTL and (c) no UTL.

are a little higher than those of TiO_2, suggesting that the TiO_2/WO_3 bilayer has a type-II energy band structure (Lu et al., 2017b; Xu et al., 2015). This helps the photo-induced carriers to transport without facing an energy barrier (Huang et al., 2017) hence avoiding charge accumulation and as a result recombination reduces (Roh et al., 2006).

In case of the SnO_2-UTL PSCs (Scheme 1(b)), the band alignment is of benefit in two respects. First, like WO_3 UTLs, the generated electrons are more easily injected because of the higher CBM edge. Second, it blocks the transfer of holes from perovskite to TiO_2 CL owing to a lower VBM (Kulkarni et al., 2016), leading to less charge recombination. Therefore, higher efficiencies obtained using the UTLs of SnO_2 compared to that of WO_3 (Fig. 5(a,b)) is related to the more effective band alignment leading to a remarkably decreased charge recombination.

3.4. Modeling with SCAPS-1D

To further study the contribution of WO_3 or SnO_2 UTLs on the electrical properties of the perovskite layer and the interfaces, the most efficient cells (the SC TiO_2 based champion cells) with the three ETL types of bare TiO_2 CL (50 nm), TiO_2 CL/SnO_2 UTL (10 nm) and TiO_2 CL/WO_3 UTL (10 nm) were modeled using Solar Cell Capacitance Simulator (SCAPS) and compared with experimental results (Fig. 7(a–c)). Due to the quantum size effects (for thicknesses less than 5 nm) (Chouchen et al., 2019; Hossain et al., 2018), the devices with 4 nm UTLs were not used in this simulation. A 1.5 AM solar radiation with a power density of 100 mW/cm^2 were used as the source of illumination and temperature was set as 300 K. In this work, an internal defect near the midgap states has been assumed for each layer. The light reflection of the front and the back contacts were set to be 0.05 and 1, respectively. The input values listed in Table 4 were used to calculate the performance of the cells. No radiative band-to-band recombination and Auger recombination are considered. The only recombination mechanism considered here is defect induced (SRH-Model). Tables S4 to S6 list the values of defect properties which are mostly obtained based on fitting.

The fittings based on the simulation results reveal that the defect formation in the bulk of the perovskite depends on the cell ETL type. Table S4 shows the concentration and energy levels of the defects. However, independent of the cell type, they remain unchanged in other layers of the device (Table S5). For the WO3-UTL cell, the energy level and the concentration of the perovskite single acceptor defects were obtained to be 0.05 eV and 7.0×10^{14} cm^{-3}, respectively. According to the literature, these values suggest that the acceptor defect I_i is dominant (Han et al., 2017). In the case of donor defects, energy level and donor concentration were found to be 1.03 eV and 4.3×10^{15} cm^{-3}, respectively which propose Pb_i is dominant. Similar quantities were obtained for the surface energy and concentration in SnO_2-UTL cell, indicating formation of similar dominant defects. In case of the bare TiO_2 device, the defect concentration is in order of 10^{10} cm^{-3}, which is negligible in comparison with UTL containing cells. There are probably unknown defects like neutral defects or clusters (Chen et al., 2013) that can affect electron affinity and optical band gap, leading to a lower absorption constant in the absorber layer (Table 4) (Niemegeers et al., 1998). Therefore, our results predict existence of new types of defects in the perovskite layer of bare TiO_2 based planar PSCs, which has been rarely noticed by scientists and reported.

The observed special photovoltaic properties of the WO_3-UTL PSCs, can be explained based on the simulation. Our modeling with WO_3 UTL shows that the defect concentration at perovskite/ETL interface is remarkably higher compared to the SnO_2-UTL or bare TiO_2 devices (Table S6). This is responsible for the lower V_{OC} and FF in the WO_3 PSCs, which has also been reported elsewhere (Eze et al., 2017; Wang et al., 2018). Our fitting results also suggest that the greater J_{SC} in WO_3 PSCs originates from a higher integral photogeneration rate (Fig. 8). This conclusion is also found in literature where the enhanced J_{SC} in the presence of WO_3 has been attributed to a fairly better behavior of the perovskite absorber layer due to its superior crystallization which leads to an increased photoabsorptions, hence an improved photogeneration rate (Wang et al., 2015).

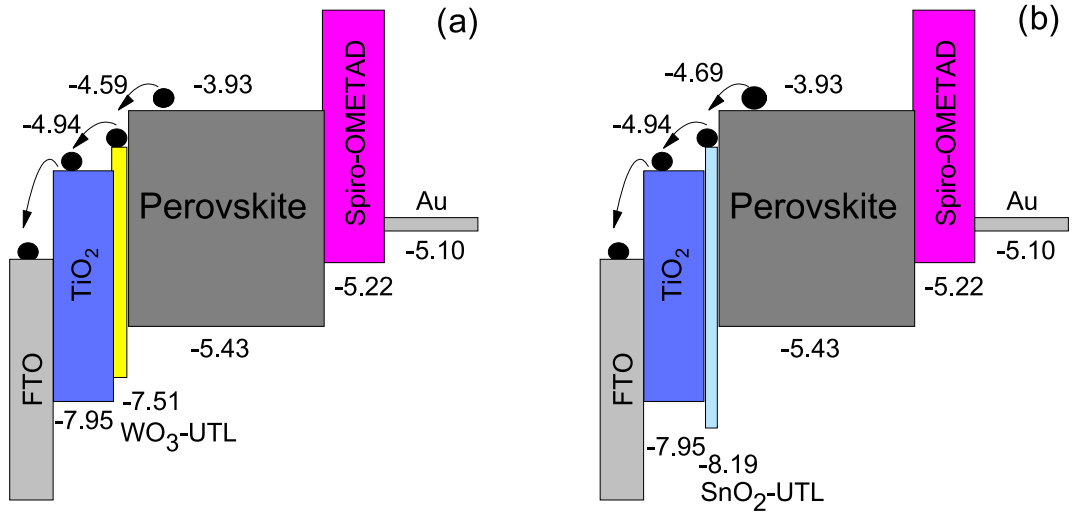

Scheme 1. The band alignment schematics of PSCs with (a) TiO_2 CL/WO_3 UTL and (b) TiO_2 CL/SnO_2 UTL bilayers.

Table 4
Basic data for the modeling case.

Parameters and units	TiO_2 CL	SnO_2 UTL	WO_3 UTL	Perovskite			HTL-Spiro
				TiO_2 CL/WO_3 UTL	TiO_2 CL/SnO_2 UTL	TiO_2 CL	
Thickness (nm)	50 (exp)*	10 (exp)	10 (exp)	550 (exp)	550 (exp)	550 (exp)	150 (exp)
Electron affinity (eV)	4.89 (exp)	4.69 (exp)	4.59 (exp)	3.93 (Shen et al., 2017)	3.93 (Shen et al., 2017)	3.7 (fitting)**,(Shen et al., 2017)	2.2 (Adhikari et al., 2016; Ng et al., 2018)
Bandgap (eV)	3.2 (exp)	3.5 (Qiu et al., 2018)	2.92 (exp)	1.5 (Shen et al., 2017)	1.5 (Shen et al., 2017)	1.65 (fitting),(Shen et al., 2017)	2.91 (Adhikari et al., 2016; Ng et al., 2018)
Dielectric permittivity (relative)	31 (Berberich and Bell, 1940)	7.25 (Yıldırım et al., 2014)	5.76 (Paliwal et al., 2014)	6.5 (Da et al., 2018)	6.5 (Da et al., 2018)	6.5 (Da et al., 2018)	3 (Shen et al., 2017)
CB effective density of states (N_C) (cm^{-3})	6.67×10^{20} (Kormann et al., 1988)	3.61×10^{18} (Button et al., 1971)	1.96×10^{19} (Berak and Sienko, 1970)	5.0×10^{18} (Shen et al., 2017)	5.0×10^{18} (Shen et al., 2017)	5.0×10^{18} (Shen et al., 2017)	1×10^{20} (Shen et al., 2017)
VB effective density of states (N_V) (cm^{-3})	6.67×10^{20} (Kormann et al., 1988)	3.61×10^{18} (Button et al., 1971)	1.96×10^{19} (Berak and Sienko, 1970)	5.0×10^{18} (Shen et al., 2017)	5.0×10^{18} (Shen et al., 2017)	5.0×10^{18} (Shen et al., 2017)	1×10^{20} (Shen et al., 2017)
Electron mobility (cm^2/Vs)	1.0×10^{-4} (Shen et al., 2017)	2.4×10^{2} (Jiang et al., 2017; Van Zeghbroeck, 1997)	10 (Berak and Sienko, 1970)	2 (Shen et al., 2017)	2 (Shen et al., 2017)	2 (Shen et al., 2017)	2 (Shen et al., 2017)
Hole mobility (cm^2/Vs)	1.0×10^{-4} (Shen et al., 2017)	2.2×10^{2} (Jiang et al., 2017; Van Zeghbroeck, 1997)	10 (Berak and Sienko, 1970)	2 (Shen et al., 2017)	2 (Shen et al., 2017)	2 (Shen et al., 2017)	1.0×10^{-2} (Shen et al., 2017)
Shallow uniform donor density (N_D) (cm^{-3})	2.81×10^{17} (exp)	2.42×10^{19} (exp)	3.68×10^{19} (exp)	0 (Shen et al., 2017)	0 (Shen et al., 2017)	0 (Shen et al., 2017)	0 (Shen et al., 2017)
Shallow uniform acceptor density (N_A) (cm^{-3})	0 (exp)	0 (exp)	0 (exp)	0 (Shen et al., 2017)	0 (Shen et al., 2017)	0 (Shen et al., 2017)	1.0×10^{18} (Shen et al., 2017)
Absorption constant A (1/cm $eV^{(1/2)}$)	1.0×10^{4} (fitting)	1.0×10^{4} (fitting)	1.0×10^{4} (fitting)	4.0×10^{4} (fitting)	4.0×10^{4} (fitting)	3×10^{4} (fitting)	1.0×10^{4} (fitting)
Absorption constant B ($eV^{(1/2)}$/cm)	0 (fitting)	0 (fitting)	0 (fitting)	0 (fitting)	0 (fitting)	0 (fitting)	0 (fitting)
Electron thermal velocity (cm/s)	1.0×10^{7} (Adhikari et al., 2016)	1.0×10^{7} (Adhikari et al., 2016)	1.0×10^{7} (Adhikari et al., 2016)	1.0×10^{7} (Adhikari et al., 2016)	1.0×10^{7} (Adhikari et al., 2016)	1.0×10^{7} (Adhikari et al., 2016)	1.0×10^{7} (Adhikari et al., 2016)
Hole thermal velocity (cm/s)	1.0×10^{7} (Adhikari et al., 2016)	1.0×10^{7} (Adhikari et al., 2016)	1.0×10^{7} (Adhikari et al., 2016)	1.0×10^{7} (Adhikari et al., 2016)	1.0×10^{7} (Adhikari et al., 2016)	1.0×10^{7} (Adhikari et al., 2016)	1.0×10^{7} (Adhikari et al., 2016)

* From our experimental measurement.
** From our fitting process.

4. Conclusions

TiO_2/SnO_2 and TiO_2/WO_3 electron transport bilayers, which combine the merits of both SnO_2 or WO_3 and TiO_2 together have been independently and successfully applied for the planar PSCs. From characterizations and simulation, the improved performance of the bilayer ETL based devices is attributed to the enhanced electron extraction, suppressed recombination rate and passivated defect states.

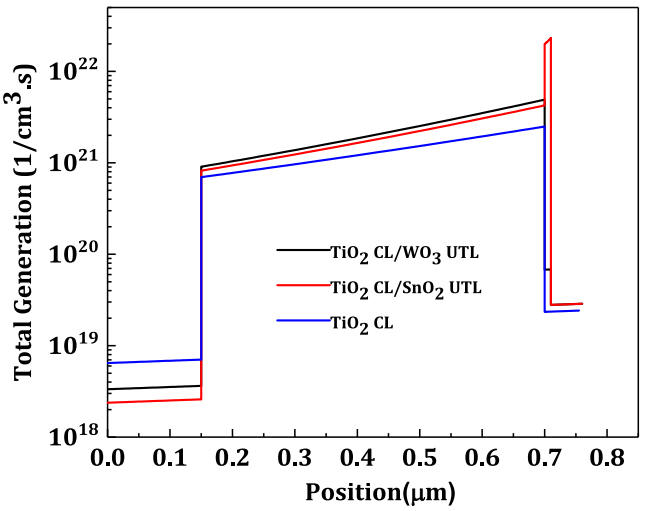

Fig. 8. A comparison between the photogeneration rates of the TiO_2 based cells.

These are consequences of improved adhesion between the perovskite and ETL, more effective band alignment and better formation of the absorber layer. To further confirming the results, the J-V curve changes were examined on similar bilayer structured PSCs based on TiO_2 CLs deposited by spin-coating and RF-sputtering, where same results were achieved. The best efficiency improvement was obtained for TiO_2-CL/SnO_2 (4 nm) bilayer (from 8.18% to 12.3%) owing to its well-aligned band structure for blocking holes. It was also revealed that thinner UTLs are more effective in PSCs with electron transport bilayer structures. The present work proved that performance of photovoltaic devices can be simply improved using the metal oxide interfacial bilayer structures.

Declaration of Competing Interest

The authors declare that they have no known competing financial interests or personal relationships that could have appeared to influence the work reported in this paper.

Acknowledgements

The authors acknowledge the central laboratory of Isfahan University of Technology (IUT) for providing RF-sputtering facilities, the Nanostructured Coating Laboratory of Sharif University of Technology for the help in conducting some of the coating and characterization tests and the Ministry of Science, Research and Technology of Iran for their partial financial support.

Research data

The SCAPS simulation data codes are available in research data with SCAPS format and additional files that give access for everyone to simulate our work.

Appendix A. Supplementary material

Supplementary data to this article can be found online at https://doi.org/10.1016/j.solener.2020.08.035.

References

Adhikari, K.R., Gurung, S., Bhattarai, B.K., Soucase, B.M., 2016. Comparative study on MAPbI3 based solar cells using different electron transporting materials. Phys. Status Solidi (c) 13 (1), 13–17.

Barsoukov, E., Macdonald, J.R., 2005. Impedance Spectroscopy Theory, Experiment, and. Applications, 2nd ed. John Wiley &Sons, Inc., Hoboken, NJ, 2005.

Berak, J.M., Sienko, M., 1970. Effect of oxygen-deficiency on electrical transport properties of tungsten trioxide crystals. J. Solid State Chem. 2 (1), 109–133.

Berberich, L., Bell, M., 1940. The dielectric properties of the rutile form of TiO2. J. Appl. Phys. 11 (10), 681–692.

Bu, T., Wu, L., Liu, X., Yang, X., Zhou, P., Yu, X., Qin, T., Shi, J., Wang, S., Li, S., 2017. Synergic interface optimization with green solvent engineering in mixed perovskite solar cells. Adv. Energy Mater. 7 (20), 1700576.

Button, K.J., Fonstad, C.G., Dreybrodt, W., 1971. Determination of the electron masses in stannic oxide by submillimeter cyclotron resonance. Phys. Rev. B 4 (12), 4539.

Chandiran, A.K., Yella, A., Mayer, M.T., Gao, P., Nazeeruddin, M.K., Grätzel, M., 2014. Sub-nanometer conformal TiO2 blocking layer for high efficiency solid-state perovskite absorber solar cells. Adv. Mater. 26 (25), 4309–4312.

Chen, B., Yang, M., Priya, S., Zhu, K., 2016. Origin of J-V hysteresis in perovskite solar cells. J. Phys. Chem. Lett. 7 (5), 905–917.

Chen, G.-S., Chen, Y.-C., Lee, C.-T., Lee, H.-Y., 2018. Performance improvement of perovskite solar cells using electron and hole transport layers. Sol. Energy 174, 897–900.

Chen, S., Walsh, A., Gong, X.G., Wei, S.H., 2013. Classification of lattice defects in the kesterite Cu2ZnSnS4 and Cu2ZnSnSe4 earth-abundant solar cell absorbers. Adv. Mater. 25 (11), 1522–1539.

Choi, J., Song, S., Hörantner, M.T., Snaith, H.J., Park, T., 2016. Well-defined nanostructured, single-crystalline TiO2 electron transport layer for efficient planar perovskite solar cells. ACS Nano 10 (6), 6029–6036.

Chouchen, B., Gazzah, M.H., Bajahzar, A., Belmabrouk, H., 2019. Numerical modeling of the electronic and electrical characteristics of InGaN/GaN-MQW solar cells. Materials 12 (8), 1241.

Christians, J.A., Schulz, P., Tinkham, J.S., Schloemer, T.H., Harvey, S.P., de Villers, B.J. T., Sellinger, A., Berry, J.J., Luther, J.M., 2018. Tailored interfaces of unencapsulated perovskite solar cells for> 1,000 hour operational stability. Nat. Energy 3 (1), 68.

Da, Y., Xuan, Y., Li, Q., 2018. Quantifying energy losses in planar perovskite solar cells. Sol. Energy Mater. Sol. Cells 174, 206–213.

Ding, B., Huang, S.-Y., Chu, Q.-Q., Li, Y., Li, C.-X., Li, C.-J., Yang, G.-J., 2018. Low-temperature SnO 2-modified TiO 2 yields record efficiency for normal planar perovskite solar modules. J. Mater. Chem. A 6 (22), 10233–10242.

El Haimeur, A., Makha, M., Bakkali, H., González-Leal, J., Blanco, E., Dominguez, M., Voitenko, Z., 2020. Enhanced performance of planar perovskite solar cells using dip-coated TiO2 as electron transporting layer. Sol. Energy 195, 475–482.

Eze, V.O., Seike, Y., Mori, T., 2017. Efficient planar perovskite solar cells using solution-processed amorphous WOx/fullerene C60 as electron extraction layers. Org. Electron. 46, 253–262.

Ganbavle, V., Agawane, G., Moholkar, A., Kim, J., Rajpure, K., 2014. Structural, optical, electrical, and dielectric properties of the spray-deposited WO3 thin films. J. Mater. Eng. Perform. 23 (4), 1204–1213.

Gedamu, D., Asuo, I.M., Benetti, D., Basti, M., Ka, I., Cloutier, S.G., Rosei, F., Nechache, R., 2018. Solvent-antisolvent ambient processed large grain size perovskite thin films for high-performance solar cells. Sci. Rep. 8 (1), 12885.

Gheno, A., Pham, T.T.T., Di Bin, C., Bouclé, J., Ratier, B., Vedraine, S., 2017. Printable WO3 electron transporting layer for perovskite solar cells: Influence on device performance and stability. Sol. Energy Mater. Sol. Cells 161, 347–354.

Gonzalez-Pedro, V., Juarez-Perez, E.J., Arsyad, W.-S., Barea, E.M., Fabregat-Santiago, F., Mora-Sero, I., Bisquert, J., 2014. General working principles of CH3NH3PbX3 perovskite solar cells. Nano Lett. 14 (2), 888–893.

Guerrero, A., Garcia-Belmonte, G., Mora-Sero, I., Bisquert, J., Kang, Y.S., Jacobsson, T.J., Correa-Baena, J.-P., Hagfeldt, A., 2016. Properties of contact and bulk impedances in hybrid lead halide perovskite solar cells including inductive loop elements. J. Phys. Chem. C 120 (15), 8023–8032.

Haghighi, M., Minbashi, M., Taghavinia, N., Kim, D.-H., Mahdavi, S.M., Kordbacheh, A. A., 2018. A modeling study on utilizing SnS 2 as the buffer layer of CZT (S, Se) solar cells. Sol. Energy 167, 165–171.

Han, D., Dai, C., Chen, S., 2017. Calculation studies on point defects in perovskite solar cells. J. Semicond. 38 (1), 011006.

Hossain, M.J., Roy, S., Hossain, M.S., Moznuzzaman, M., 2018. Analytical modeling of AlInN/GaN quantum dot intermediate band solar cell. In: 2018 International Conference on Innovation in Engineering and Technology (ICIET). IEEE, pp. 1–5.

Huang, X., Hu, Z., Xu, J., Wang, P., Wang, L., Zhang, J., Zhu, Y., 2017. Low-temperature processed SnO 2 compact layer by incorporating TiO 2 layer toward efficient planar heterojunction perovskite solar cells. Sol. Energy Mater. Sol. Cells 164, 87–92.

Jiang, Q., Zhang, L., Wang, H., Yang, X., Meng, J., Liu, H., Yin, Z., Wu, J., Zhang, X., You, J., 2017. Enhanced electron extraction using SnO 2 for high-efficiency planar-structure HC (NH 2) 2 PbI 3-based perovskite solar cells. Nat. Energy 2 (1), 16177.

Ke, W., Fang, G., Wan, J., Tao, H., Liu, Q., Xiong, L., Qin, P., Wang, J., Lei, H., Yang, G., 2015. Efficient hole-blocking layer-free planar halide perovskite thin-film solar cells. Nat. Commun. 6, 6700.

Kogo, A., Ikegami, M., Miyasaka, T., 2016. A SnO x–brookite TiO 2 bilayer electron collector for hysteresis-less high efficiency plastic perovskite solar cells fabricated at low process temperature. Chem. Commun.

Kormann, C., Bahnemann, D.W., Hoffmann, M.R., 1988. Preparation and characterization of quantum-size titanium dioxide. J. Phys. Chem. 92 (18), 5196–5201.

Kulkarni, A., Jena, A.K., Chen, H.-W., Sanehira, Y., Ikegami, M., Miyasaka, T., 2016. Revealing and reducing the possible recombination loss within TiO2 compact layer by incorporating MgO layer in perovskite solar cells. Sol. Energy 136, 379–384.

Li, J., Wu, N., 2015. Semiconductor-based photocatalysts and photoelectrochemical cells for solar fuel generation: a review. Catal. Sci. Technol. 5 (3), 1360–1384.
Li, Y., Zhu, J., Huang, Y., Liu, F., Lv, M., Chen, S., Hu, L., Tang, J., Yao, J., Dai, S., 2015. Mesoporous SnO 2 nanoparticle films as electron-transporting material in perovskite solar cells. RSC Adv. 5 (36), 28424–28429.
Lim, S., Huang, N.M., Lim, H.N., Mazhar, M., 2014. Surface modification of aerosol-assisted CVD produced TiO2 thin film for dye sensitised solar cell. Int. J. Photoenergy 2014.
Lu, G., He, F., Pang, S., Yang, H., Chen, D., Chang, J., Lin, Z., Zhang, J., Zhang, C., 2017. A PCBM-modified TiO2 blocking layer towards efficient perovskite solar cells. Int. J. Photoenergy 2017.
Lu, H., Tian, W., Gu, B., Zhu, Y., Li, L., 2017b. TiO2 electron transport bilayer for highly efficient planar perovskite solar cell. Small 13 (38), 1701535.
Mohammadian-Sarcheshmeh, H., Mazloum-Ardakani, M., 2018. Recent advancements in compact layer development for perovskite solar cells. Heliyon 4 (11), e00912.
Ng, C.H., Ripolles, T.S., Hamada, K., Teo, S.H., Lim, H.N., Bisquert, J., Hayase, S., 2018. Tunable open circuit voltage by engineering inorganic cesium lead bromide/iodide perovskite solar cells. Sci. Rep. 8 (1), 2482.
Niemegeers, A., Gillis, S., Burgelman, M., 1998. A user program for realistic simulation of polycrystalline heterojunction solar cells: SCAPS-1D. In: Proceedings of the 2nd World Conference on Photovoltaic Energy Conversion, JRC, European Commission, juli. pp. 672-675.
Noh, M.F.M., Teh, C.H., Daik, R., Lim, E.L., Yap, C.C., Ibrahim, M.A., Ludin, N.A., bin Mohd Yusoff, A.R., Jang, J., Teridi, M.A.M., 2018. The architecture of the electron transport layer for a perovskite solar cell. J. Mater. Chem. C 6(4), 682–712.
NREL, 2019. NREL, 2019. Solar Cell Efficiency Chart <https://www.nrel.gov/pv/cell-efficiency.html>.
Paliwal, A., Sharma, A., Tomar, M., Gupta, V., 2014. Optical properties of WO3 thin films using surface plasmon resonance technique. J. Appl. Phys. 115 (4), 043104.
Qiu, L., Liu, Z., Ono, L.K., Jiang, Y., Son, D.Y., Hawash, Z., He, S., Qi, Y., 2018. Scalable fabrication of stable high efficiency perovskite solar cells and modules utilizing room temperature sputtered SnO2 electron transport layer, 1806779 Adv. Funct. Mater.
Reyes-Coronado, D., Rodríguez-Gattorno, G., Espinosa-Pesqueira, M., Cab, C., de Coss, R. d., Oskam, G., 2008. Phase-pure TiO2 nanoparticles: anatase, brookite and rutile. Nanotechnology 19(14), 145605.
Roh, S.-J., Mane, R.S., Min, S.-K., Lee, W.-J., Lokhande, C., Han, S.-H., 2006. Achievement of 4.51% conversion efficiency using ZnO recombination barrier layer in Ti O 2 based dye-sensitized solar cells. Appl. Phys. Lett. 89 (25), 253512.
Saliba, M., Matsui, T., Seo, J.-Y., Domanski, K., Correa-Baena, J.-P., Nazeeruddin, M.K., Zakeeruddin, S.M., Tress, W., Abate, A., Hagfeldt, A., 2016. Cesium-containing triple cation perovskite solar cells: improved stability, reproducibility and high efficiency. Energy Environ. Sci. 9 (6), 1989–1997.
Shen, H., Jacobs, D.A., Wu, Y., Duong, T., Peng, J., Wen, X., Fu, X., Karuturi, S.K., White, T.P., Weber, K., 2017. Inverted hysteresis in CH3NH3PbI3 solar cells: role of stoichiometry and band alignment. J. Phys. Chem. Lett. 8 (12), 2672–2680.
Swanepoel, R., 1984. Determination of surface roughness and optical constants of inhomogeneous amorphous silicon films. J. Phys. E: Sci. Instrum. 17 (10), 896.
Van Zeghbroeck, B.J., 1997. Bravais Lattices. Principles of Semiconductor Devices.
Wang, F., Bai, S., Tress, W., Hagfeldt, A., Gao, F., 2018. Defects engineering for high-performance perovskite solar cells. npj Flexible. Electronics 2 (1), 1–14.
Wang, J.-F., Zhu, L., Zhao, B.-G., Zhao, Y.-L., Song, J., Gu, X.-Q., Qiang, Y.-H., 2017. Surface engineering of perovskite films for efficient solar cells. Sci. Rep. 7 (1), 1–9.
Wang, K., Shi, Y., Dong, Q., Li, Y., Wang, S., Yu, X., Wu, M., Ma, T., 2015. Low-temperature and solution-processed amorphous WO X as electron-selective layer for perovskite solar cells. J. Phys. Chem. Lett. 6 (5), 755–759.
Xu, X., Zhang, H., Shi, J., Dong, J., Luo, Y., Li, D., Meng, Q., 2015. Highly efficient planar perovskite solar cells with a TiO 2/ZnO electron transport bilayer. J. Mater. Chem. A 3 (38), 19288–19293.
Yang, D., Zhou, X., Yang, R., Yang, Z., Yu, W., Wang, X., Li, C., Liu, S.F., Chang, R.P., 2016a. Surface optimization to eliminate hysteresis for record efficiency planar perovskite solar cells. Energy Environ. Sci. 9 (10), 3071–3078.
Yang, G., Tao, H., Qin, P., Ke, W., Fang, G., 2016b. Recent progress in electron transport layers for efficient perovskite solar cells. J. Mater. Chem. A 4 (11), 3970–3990.
Yıldırım, M.A., Yıldırım, S.T., Sakar, E.F., Ateş, A., 2014. Synthesis, characterization and dielectric properties of SnO2 thin films. Spectrochim. Acta Part A Mol. Biomol. Spectrosc. 133, 60–65.